J Mater Sci: Mater Electron (2015) 26:6793–6800
DOI 10.1007/s10854-015-3291-x

Transport properties of Ba-doped $BiFeO_3$ multiferroic nanoparticles

M. M. El-Desoky[1] · M. M. Mostafa[1] · M. S. Ayoub[1] · M. A. Ahmed[2]

Received: 23 April 2015 / Accepted: 29 May 2015 / Published online: 3 June 2015

Abstract Multiferroic nanoparticles of $Bi_{1-x}Ba_xFeO_3$ ($BiBaFeO_3$); ($x = 0.10$, 0.15, 0.20 and 0.25 mol%) samples were prepared using conventional solid-state method. The nanostructural and transport properties of the prepared samples were investigated by X-ray diffraction (XRD), scanning electron microscope (SEM) and electrical conductivity. XRD patterns show the formation of $BiBaFeO_3$ with single-phase rhombohedral-hexagonal structure. The particles sizes were found to be in the range 20–33 nm. SEM micrograph revealed the nanostructure consisting of small, randomly oriented and non-uniform grains. Dc conductivity shows that all samples are semiconductor and the maximum was found at $x = 0.15$ mol%. This increase of the conductivity can be attributed to the decrease in grain boundary scattering due to the reduction in crystallite size. The calculated activation energy for the multiferroic nanoparticles was found to be 0.413–0.929 eV. The conduction was confirmed to obey non-adiabatic small polaron hopping (SPH). The electron–phonon interaction coefficient (γ_p) was calculated and found to be in the range of (12.79–27.21). The hopping carrier mobility varied from 1.85×10^{-7} $cm^2V^{-1}s^{-1}$ to 8.01×10^{-13} $cm^2V^{-1}s^{-1}$ at 418 K. The conductivity was primarily determined by hopping carrier mobility.

✉ M. M. El-Desoky
mmdesoky@gmail.com; mmdesoky@suezuniv.edu.eg

[1] Physics Department, Faculty of Science, Suez University, Suez, Egypt

[2] Materials Science Lab (1), Physics Department, Faculty of Science, Cairo University, Giza, Egypt

1 Introduction

Multiferroics have attracted much attention in recent years because of a wide range of potential applications in magnetic data storage, logic devices, spintronic devices, and sensors [1, 2]. $BiFeO_3$ is single phase material which shows multiferroic behavior at room temperature having high ferroelectric Curie temperature ($T_C \sim 1100$ K) and antiferromagnetic Néel temperature ($T_N \sim 640$ K) [3]. It possesses rhombohedral distorted perovskite (ABO_3) structure [4]. The ferroelectricity and magnetism in $BiFeO_3$ is attributed to the Bi^{3+} $6s^2$ lone pair electrons and partially filled d orbital of Fe^{3+} ion, respectively [5], thus the coupling between the ferroelectric and magnetic ordering is usually considered to be rather weak [6]. However, the importance of multiferroic materials, no experimental work discussed the mechanism of dc conductivity for $BiBaFeO_3$ multiferroic nanoparticles in detail so far, to the best of our knowledge. It seems to be interesting to investigate the detail electrical conductivity and small polaron hopping mechanism because of the multiferroic materials such as $BiFeO_3$ have focused on the role of strong electron–phonon coupling leading to the formation of polarons.

Large number of oxygen vacancies produced because of bismuth which has highly volatile nature and the multiple oxidation states of iron (Fe^{2+} and Fe^{3+}) cause a high leakage current in the material that limits its multiferroic properties [7]. Leakage current due to oxygen vacancies or impurities is the major problem in $BiFeO_3$. It has been observed that doping at A-sites reduce the leakage current in $BiFeO_3$ and enhance the multiferroic properties [8]. The substitution of Bi^{3+} by Ba^{2+} may cause two parallel phenomena with respect to the concentration of oxygen vacancies: (1) the creation of oxygen vacancies to neutralize the charge produced substituting Bi^{3+} by Ba^{2+}, and

(2) decrease in concentration of oxygen vacancies by filling the probable vacant volatilized Bi^{3+} sites [9].

Polaron hopping theory [10] was used to illustrate transport mechanism in undoped or doped semiconductors where electrons are localized by potential fluctuations associated with the dopant. A strong electron–phonon interaction is considered to be responsible for the formation of small polarons [11] and the polaron hopping conduction model has been used to illustrate the semiconducting behavior. The semiconducting properties of transition metal oxide (TMO) arise from the presence of different valence states of transition metal ions [12–17].

The conduction occurs by the hopping movement between two different states of the iron in the temperatures higher than $\theta_D/2$ (θ_D: Debye temperature) [18]. The charge transfer is usually termed small polaron hopping (SPH) [19]. The electrical conductivity depends strongly upon the local interaction of an electron with its surroundings and the distance between the iron ions [15, 20–22]. In case of $BiBaFeO_3$ multiferroic nanoparticles, the charge carrier concentration is related to the total concentration of iron ions and to the ratio of Fe^{2+} ions to the total quantity of iron (Fe^{2+} /ΣFe) [14].

In the present work, we have synthesized $Bi_{1-x}Ba_xFeO_3$; ($0.10 \leq x \leq 0.25$ mol%) multiferroic nanoparticles, and investigated on the effect of Ba^{2+} ions substitution on the structural and transport behavior of $BiFeO_3$ samples.

2 Experimental

Nanometric samples with having the chemical formula $Bi_{1-x}Ba_xFeO_3$ ($BiBaFeO_3$); ($x = 0.10$, 0.15, 0.20 and 0.25 mol%) were prepared by the conventional solid-state reaction from analar grade form oxides (BDH), including Bi_2O_3, $BaCO_3$ and Fe_2O_3. Stoichiometric ratios of pure oxides, with purity 99.99 %, were good mixed and ground using agate mortar for 3.5 h. The samples were pressed into pellet form using uniaxial press. Presintering was carried out in air at 600 °C for 6 h using a heating rate of 4 °C/min. The samples were cooled to room temperature with the same above rate; regrinded for 1.5 h. Final sintering was carried out at 850 °C for 3 h with the same above rate in open atmosphere. The prepared samples were checked by X-ray diffraction using Diano corporation of target Co-Kα ($\lambda = 1.79026$ Å) to assure the complete reaction and the formation of single-phase structure. The morphology of the sample ($x = 0.20$ %) as a representative sample was investigated by scanning electron microscope (SEM), Model Quanta 250 FEG (Field Emission Gun). The dc conductivity was measured as a function of barium content and temperature by the two-probe method using silver past electrodes. A multimeter type (ISO-TECHIDM 303) was used to collect the dc data. The samples in the form of pellets were coated with conducting colloidal silver and held between the electrodes of a conductive stainless steel cell. The conductivity measurements were performed over a temperature range from 300 to 590 K.

3 Results and discussions

3.1 Characterization

3.1.1 X-ray diffraction (XRD)

Figure 1 shows XRD patterns for $Bi_{1-x}Ba_xFeO_3$ ($BiBaFeO_3$); ($x = 0.10$, 0.15, 0.20 and 0.25 mol%) multiferroic nanoparticles at room temperature. As shown in Fig. 1, the appearance of strong reflection from (110), (024), (012), (214) and (202). The diffraction peaks of $BiBaFeO_3$ samples can be indexed to the hexagonal unit cell (with space group R3c) which agrees with the results reported by Jaiparkash et al. [23]. Where the broad XRD peaks confirm that the samples are in nanocrystalline form. The average crystallite size of the nanoparticles has been calculated using the Debye–Scherrer equation

$$D = \frac{k\lambda}{\beta cos\theta} \quad (1)$$

where D is the crystallite size in Å, $k = 0.89$ is the correction factor, λ is the Cu target wavelength, β is the full width half maximum (FWHM) of the most intense peak and θ is the angle of diffraction. Small intensities of a secondary phases were observed for $x = 0.10$ mol%. These phases were indexed as $Bi_2Fe_4O_9$ and $BaFe_2O_4$ and with addition of Ba^{2+} ions; the impurity peaks of $Bi_2Fe_4O_9$

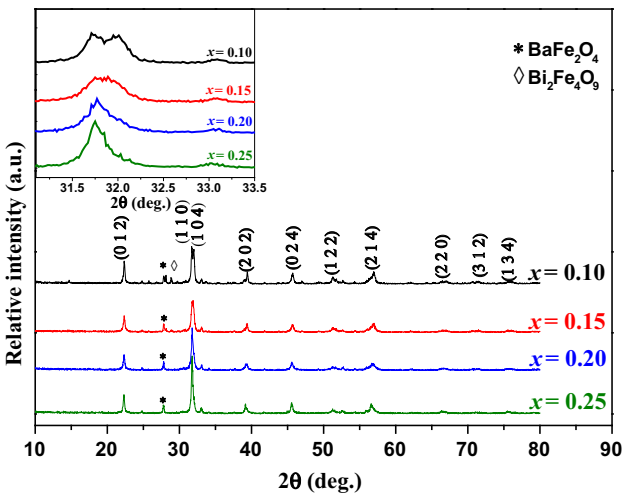

Fig. 1 X-ray diffraction pattern for $Bi_{1-x}Ba_xFeO_3$ multiferroic nanoparticles at room temperature

are vanished. To examine the effect of Ba^{2+} ions substitution on the structure, as can be seen clearly in the inset Fig. 1, with increasing Ba^{2+} ions substitution, the diffraction peaks of (104) and (110) merge to one peak for $x = 0.15$ mol%. The average value of FWHM as shown from Fig. 1 has a maximum value at $x = 0.15$ mol%, it is indicating that the distortion in the system is maximum for $x = 0.15$ mol% [23]. In addition, the crystallite size is small which change cycloidal spin structure to a canted spin structure [24]. The crystallite sizes of present samples are summarized in Table 1.

From XRD results, the lattice parameters (a and c) were computed based on hexagonal unit cell (with space group R3c) and listed in Table 1 using the relation [23]

$$\frac{1}{d^2} = \frac{4}{3}\frac{(h^2 + hk + k^2)}{a^2} + \frac{l^2}{c^2} \quad (2)$$

where d is the inter-planar spacing and (h k l) are miller indices. It is clearly observed from the tabulated parameters that the lattice parameters increase slightly with increasing barium content obeying the well-known Vegard's law [25] and improvement in the volume (V) of the unit cell. The theoretical density (ρ) was calculated from the equation

$$\rho = \frac{ZM}{N_A V} \quad (3)$$

where Z is the number of molecules per unit cell, M is the molecular weight and N_A is the Avogadro's number [25]. It is clear that density decreases with increasing barium content. The density for these samples was consistent with the ionic size, atomic weight and amount of different elements in the samples as listed in Table 1.

3.1.2 Scanning electron microscope (SEM)

Figure 2 shows SEM micrograph of $x = 0.20$ mol% multiferroic nanoparticle sample revealed the nanostructure consisting of small, randomly oriented and non-uniform grains (as shape and size), which affects the sample density. The variation of grain morphologies may be an evidence of the formation of impurity phases. Figure 2 appears an agglomeration process as a result of electrostatic potential and magnetic attraction. This is a result of an abnormal/discontinuous grain growth and called an exaggerated grain growth. In the abnormal grain growth, with increasing sintering temperature some grains grow faster than others. The abnormal growth may be obtained from: (1) the existence of second phase impurities or precipitates, (2) materials, which have high anisotropy in interfacial energy and (3) materials in high chemical in equilibrium [26]. It can be assumed that the abnormal growth for $BiBaFeO_3$, which crystallizes in rhombohedral–hexagonal structure, comes from (1) and (3) [27]. This type of grain structure as shown in Fig. 2 is common in oxide, ferrite and titanate ceramics [28].

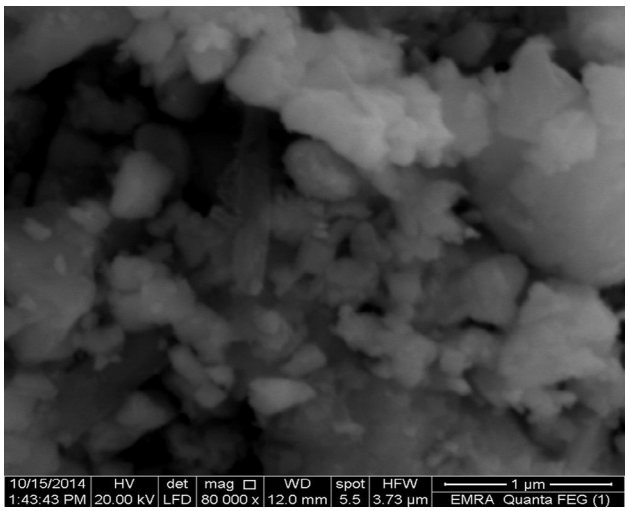

Fig. 2 SEM micrograph of the multiferroic nanoparticle sample for x = 0.20 mol%

3.2 Dc electrical conductivity

Figure 3 shows the variations of dc conductivity (σ_{dc}) of $BiBaFeO_3$ multiferroic nanoparticles as a function of reciprocal of the absolute temperature. It is clearly seen that a linear temperature dependence up to a critical temperature $\theta_D/2$ (θ_D: Debye temperature) and then the slope changes with deviation from linearity and the activation energy is temperature dependent, indicating that the dc conductivity obeys Arrhenius relation.

$$\sigma = \sigma_o \exp(-E_a/k_B T) \quad (4)$$

where σ_o is the pre-exponential factor, E_a is the activation energy and k_B is Boltzmann's constant and T is the absolute

Table 1 Particle size, lattice parameters and density of $Bi_{1-x}Ba_xFeO_3$ multiferroic nanoparticles at room temperature

x (mol%)	D (nm) ± 1	a (Å)	c (Å)	c/a	V (Å^3)	ρ (g/cm^3) ± 0.01
0.10	33	5.609	13.673	2.438	372.50	8.17
0.15	20	5.616	13.655	2.432	372.98	8.07
0.20	23	5.621	13.713	2.440	375.15	7.93
0.25	30	5.630	13.786	2.449	378.37	7.76

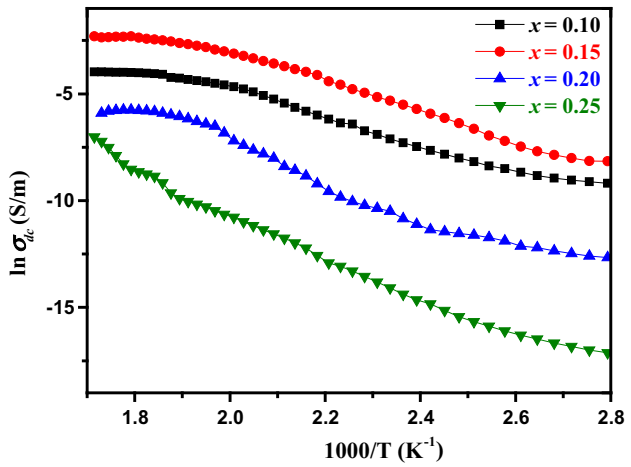

Fig. 3 Variation of dc conductivity (ln σ_{dc}) as a function of inverse of temperature (T^{-1}) for $Bi_{1-x}Ba_xFeO_3$ multiferroic nanoparticles

temperature. E_a was calculated from the slope of curve for all multiferroic nanoparticles samples above critical temperature ($\theta_D/2$) which Debye temperature in the range 745–776 K. The pre-exponential factor (σ_o) was obtained from the interception of the least square straight-line fits of the data. It is obvious that σ_{dc} increases with increase in temperature, indicating a semiconducting nature of the different $BiBaFeO_3$ multiferroic nanoparticles.

Figure 4 shows the variation of dc conductivity and crystallite size as a function of barium content. The maximum conductivity and minimum crystallite size was found for $x = 0.15$ mol% as shown in Fig. 4. This maximum conductivity may be due to the reduction in crystallite size. However, the electrical conductivity is affected by grain boundary scattering. This grain boundaries act as traps which capture electrons and lead to the formation of a potential barrier. Building up of a potential barrier at the grain boundaries also causes scattering of conduction electrons, which decreases the conductivity. So, the increase of the conductivity can be attributed to the decrease in grain boundary scattering due to the reduction in crystallite size [29].

The electrical conductivity is affected by grain boundary scattering. The increase of the conductivity can be attributed to the decrease in grain boundary scattering due to the reduction in crystallite size.

Figure 5 illustrates the variation of dc conductivity and activation energy as a function of barium content. A general trend observed in Fig. 5 is that the magnitude of the conductivity at fixed temperature (418 K) tends to be highest having smallest activation energy, which is consistent with small polaron hopping conduction mechanism (SPH) in transition metal oxide (TMO). Such behavior arises from the hopping of polarons or electrons between mixed valance states [19, 30, 31]. Therefore, the experimental conductivity data above $\theta_D/2$ were fitted with SPH model proposed by Mott [32]. On the other hand, the decrease in σ_{dc} and increase in E_a with increasing barium content, this can be explained as incorporation of barium ion creates a large lattice distortion in bismuth ferrite lattice, which will increase the effective potential barrier height for charge carrier contribution in conduction process [33].

3.2.1 *Nature of conduction mechanism*

Mott [34] has investigated the hopping conductivity in TMO. If the interaction between electrons and optical phonons is strong enough, a small polaron will be formed and at sufficiently high temperatures, this will move by hopping process [22].

In the non-adiabatic hopping regime, when the electron has a low chance of making the transfer during each

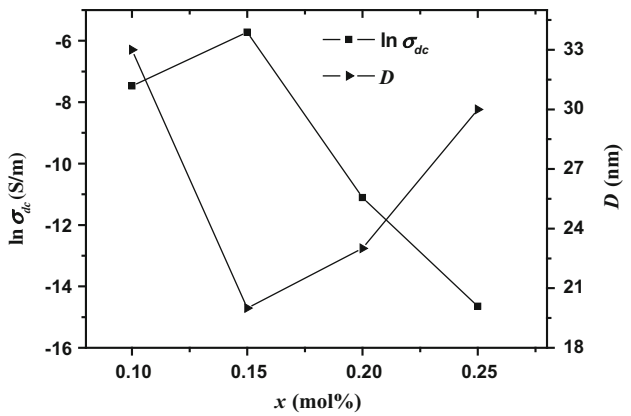

Fig. 4 Effect of barium content (x) on dc conductivity (ln σ_{dc}) at fixed temperature (418 K) and crystallite size (D) for $Bi_{1-x}Ba_xFeO_3$ multiferroic nanoparticles

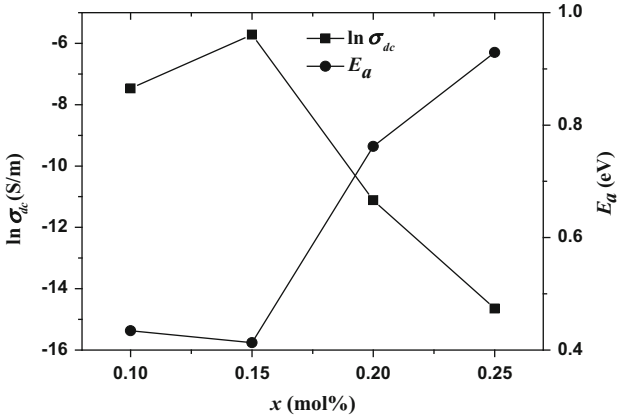

Fig. 5 Effect of barium content (x) on dc conductivity (ln σ_{dc}) and activation energy (E_a) at fixed temperature (418 K) for $Bi_{1-x}Ba_xFeO_3$ multiferroic nanoparticles

excitation. The conductivity of the nearest neighbor at high temperatures ($T > \theta_D/2$) is given by

$$\sigma = \upsilon_o N e^2 R^2 C(1-C)\exp(-2\alpha R)\exp(-E_a/kT) \quad (5)$$

The pre-exponential factor σ_o in Eq. 5 is given by

$$\sigma_o = \upsilon_o N e^2 R^2 C(1-C)\exp(-2\alpha R) \quad (6)$$

where α the tunneling factor, R mean distance between iron ions, N the transition metal density, C the fraction of reduced transition metal ion ($C = Fe^{2+}/\Sigma Fe$), e the electronic charge, E_a is the activation energy for hopping conduction and υ_o is the optical phonon frequency which measured from the electrical conductivity data, according to the formula ($k\theta_D = h\upsilon_o$) and obtained to be 1.553–1.618 $\times$ 10^{13} Hz.

Assuming a strong electron–phonon interaction, Austin and Mott [35] have shown that

$$E_a = W_H + W_D/2 \quad \text{for } (T > \theta_D/2) \quad (7)$$

$$E_a = W_D \quad \text{for } (T > \theta_D/4) \quad (8)$$

where W_H (=W_p/2) is the polaron hopping energy and W_D the disorder energy defined as the difference of electronic energies between two hopping sites.

$$W_D = \left(e^2 R/\varepsilon_o \varepsilon_s\right)L \quad (9)$$

where ε_s is the static dielectric constant and L is a constant of order 0.3. The values of W_D and E_a are summarized in Tables 2 and 3.

In the adiabatic hopping regime, the electron goes backward and forward several times during each excitation of the lattice. However, αR in Eqs. 5 and 6 becomes negligible [22, 34, 35], then the conductivity σ and the pre-exponential factor σ_o in Eqs. 5 and 6 are expressed by the following equations [34, 35]

$$\sigma = \upsilon_o N e^2 R^2 C(1-C)\exp(-E_a/kT) \quad (10)$$

and

$$\sigma_o = \upsilon_o N e^2 R^2 C(1-C) \quad (11)$$

The nature of polaron hopping mechanism (adiabatic or non-adiabatic) can be estimated from a plot of ln σ against activation energy at fixed experimental temperature T [33]. It is expected that the hopping will be in the adiabatic regime if the temperature estimated T_e, from the slope of such a plot, is close to the experimental temperature T. Otherwise the hopping will be in the non-adiabatic regime.

In Fig. 3, it is observed that the magnitude of the conductivity at all temperatures tends to be the highest for those samples having the lowest thermal activation energy. This is consistent qualitatively with Eq. 5 proposed for polaron hopping at high temperatures. A relationship between σ versus E_a for all samples at fixed temperature (418 K) is shown in Fig. 6. It might be noted that the data fall on a straight line for the entire interval of E_a. From the slope of the plot, the value of temperature (T_e = 753 K) is estimated, which is very different from the temperature chosen (T = 418 K). Figure 7 presents the effect of barium content on the pre-exponential factors obtained from the least squares straight line fits of the data (σ_o) indicating a decrease in σ_o with barium content increased from 10 to 25 mol%. For both these results, we conclude the conduction mechanism in the present samples to be due to non-adiabatic SPH of electrons [35].

3.2.2 *Relation between activation energy and mean distance between iron ions*

The concentration of iron ions per unit volume N (cm^{-3}) was estimated using the density by the relation

$$N = \rho p N_A/(A_w \times 100) \quad (12)$$

where ρ is the density of the sample, p is the weight percentage of atoms, N_A is the Avogadro's constant and A_w is the atomic number. The mean distance R between iron ions was calculated from

$$R = (1/N)^{1/3} \quad (13)$$

The values of R and N are listed in Table 2. The change in the R with increasing barium content was illustrated in terms of the structural changes that take place. The relation between the activation energy E_a and the mean distance R between iron ions is shown in Fig. 8. In the range of measurements, E_a depends on the site-to-site distance R. This result shows that there is a prominent positive correlation between E_a and R between iron ions. The effect dependence of σ on the barium content can be explained by changes in the distance between the iron ions, R.

The minimum activation energy was found for x = 0.15 mol% as shown in Fig. 8. This minimum activation

Table 2 Physical properties of $Bi_{1-x}Ba_xFeO_3$ multiferroic nanoparticles at fixed temperature (418 K)

x (mol%)	lnσ (S/m) ± 0.01	lnσ_o (S/m) ± 0.01	$N \times 10^{22}$ (cm^{-3})	R (nm)	E_a (eV) ± 0.01
0.10	−7.47	−3.80	1.610	0.3960	0.44
0.15	−5.72	−2.99	1.608	0.3962	0.41
0.20	−11.11	−5.72	1.599	0.3969	0.76
0.25	−14.65	−6.15	1.585	0.3981	0.93

Table 3 Small polaron hopping parameters of $Bi_{1-x}Ba_xFeO_3$ multiferroic nanoparticles at fixed temperature (418 K)

x (mol%)	W_H (eV) ± 0.01	W_D (eV)	r_p (nm)	ε_p	$N(E_F) \pm 10^{21}$ (cm^{-3})	$\gamma_p \pm 0.01$
0.10	0.432	0.0048	0.1596	842	8.84	13.23
0.15	0.411	0.0046	0.1597	1146	9.29	12.79
0.20	0.758	0.0085	0.1600	806	5.01	23.28
0.25	0.911	0.0374	0.1604	398	4.07	27.20

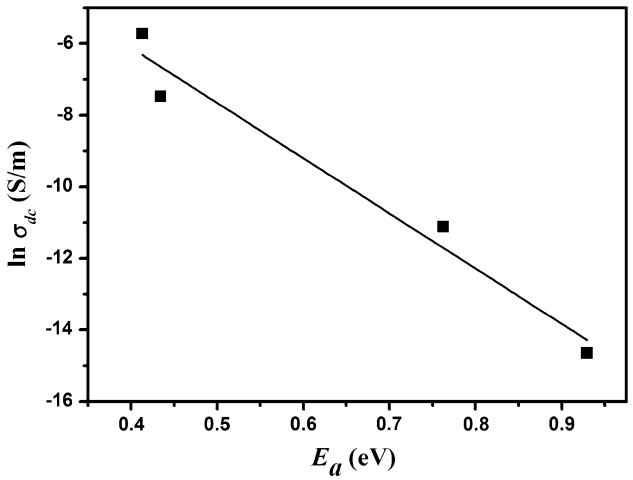

Fig. 6 Effect of activation energy (E_a) on dc conductivity (ln σ_{dc}) at fixed temperature (418 K) for different $Bi_{1-x}Ba_xFeO_3$ multiferroic nanoparticles

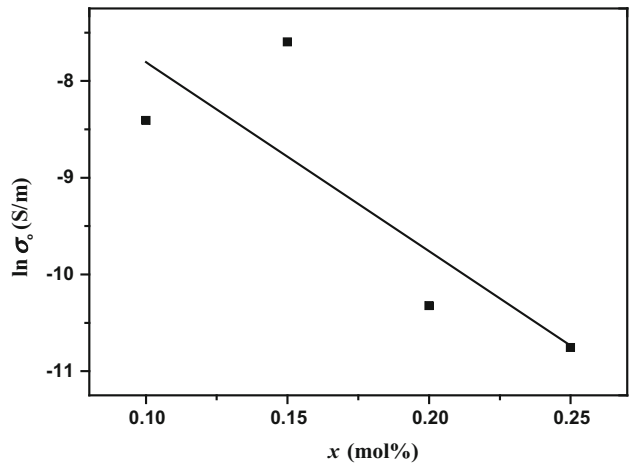

Fig. 7 Effect of barium content (x) on pre-exponential factor (ln σ_o) for $Bi_{1-x}Ba_xFeO_3$ multiferroic nanoparticles

energy may be attributed to the decrease in grain boundary scattering. On the other hand, with increasing barium content, the calculated distance between the iron ions increases from 0.3960 to 0.3981 nm and the decrease in σ is attributed to increase in the distance R between iron ions. It is concluded, therefore, that the conduction between iron ions depends strongly on R, which is important to the conduction mechanism of these multiferroic nanoparticle

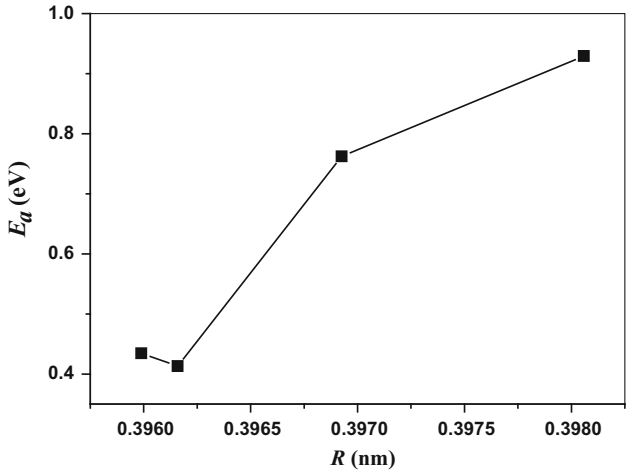

Fig. 8 Effect of the average distance (R) on activation energy (E_a) at fixed temperature (418 K) for different $Bi_{1-x}Ba_xFeO_3$ multiferroic nanoparticles

samples. This agrees with the results obtained by M. M. El-Desoky et al. [29, 36].

3.2.3 *Nature of small polaron hopping (SPH) conduction*

In SPH conduction, the polaron bandwidth (J) or the electron overlap integral obeys [17].

$$J > \left(\frac{2kTW_H}{\pi}\right)^{1/4}\left(\frac{\hbar\upsilon_o}{\pi}\right)^{1/2} \quad \text{(adiabatic)} \tag{14}$$

$$J < \left(\frac{2kTW_H}{\pi}\right)^{1/4}\left(\frac{\hbar\upsilon_o}{\pi}\right)^{1/2} \quad \text{(non-adiabatic)} \tag{15}$$

This model also provides an independent way of ascertaining the nature of hopping mechanism at high temperatures. The condition for formation of small polaron is given by [35].

$$J < W_H/3 \tag{16}$$

the limiting value of J calculated from the right-hand side ($R.H.S$) of expression 14 or 15 at fixed temperature (418 K) is of the order of 0.0178–0.0221 eV, depending on barium content and therefore the condition for the existence of small polaron is satisfied. An unambiguous decision as to whether the polaron is actually in the adiabatic or

in the non-adiabatic regime requires an estimate of the value of J, which can be obtained from [17]

$$J \approx e^3 \left[N(E_F) / \left(\varepsilon_o \varepsilon_p \right)^3 \right]^{1/2} \quad (17)$$

where

$$\frac{1}{\varepsilon_p} = \frac{1}{\varepsilon_\infty} - \frac{1}{\varepsilon_s} \quad (18)$$

where ε_s and ε_∞ are the static and high frequencies dielectric constants of the samples, respectively. ε_s was taken at 5 kHz while ε_∞ was taken at 400 kHz. ε_p is effective dielectric permittivity. Using the values of $N(E_F)$ and ε_p from Table 3, Eq. 17 gives $J \approx 0.0106$ eV, these values of J are much smaller than those estimated from the *R.H.S* of Eq. 15 and thus the non-adiabatic hopping theory is most appropriate to describe the polaronic conduction at high temperatures in the present samples.

3.2.4 Small polaron hopping (SPH) parameters

For adiabatic hopping conduction, the hopping energy, W_H, is given using J as

$$E_a - W_D/2 \simeq W_H = W_p/2 = W_p'/2 - J \quad (19)$$

where W_p is the polaron binding energy, $W_p^{'}$ is the maximum polaron binding energy and W_H depends on R [37]. By contrast, for non-adiabatic hopping conduction, W_H is given as follows

$$E_a - W_D/2 \simeq W_H = W_p'/2 \quad (20)$$

In order to determine W_H value of the present samples, we evaluated the disorder energy, W_D (Table 3) and activation energy, E_a (Table 2). W_D at room temperature is recognized as generally to be below 0.1 eV [17]. For the present system within the test temperature range, W_D is assumed here to be 0.0046–0.0374 eV, as described in Table 3, we then obtain $W_H = 0.411$–0.911 eV. For the present samples, W_H is nearly equal to E_a.

Next, using the mean spacing between the iron ions, R, calculated from the density (Table 2), polaron radius (r_p) is given by [17].

$$r_p = (\pi/6)^{1/3} R/2 \quad (21)$$

r_p was then estimated to be $r_p = 0.1596$–0.1604 nm (Table 3) from $R = 0.3960$–0.3981 nm (Table 2).

The density of states for thermally activated electron hopping near the Fermi level $N(E_F)$ is given from basic principles as [15, 22].

$$N(E_F) = \left(3/4\pi R^3 E_a \right) \quad (22)$$

Using R and E_a values from Table 2, one can calculate $N(E_F)$ for the present samples. It is clear that, the density of states $N(E_F)$ is the order of 10^{21} ($\mathrm{eV}^{-1}\mathrm{cm}^{-3}$) [14, 15]. The values of $N(E_F)$ are listed in Table 3. The $N(E_F)$ values are reasonable for the localized states [14, 15].

The values of small polaron coupling constant (γ_p), a measure of electron–phonon interaction, given by the formula

$$\gamma_p = 2W_H/h\upsilon_o \quad (23)$$

were also evaluated for the present samples [18]. The estimated values of γ_p are listed in Table 3. The value of $\gamma_p > 4$ usually indicates a strong electron–phonon interaction [22]. From results listed in Table 3, we can deduce the value of r_p is increasing slightly with increasing barium content and the values of W_H and γ_p have inflection point (minimum peak) at $x = 0.15$ mol%. This meaning the polaron hopping energy and electron–phonon interaction is minimum for $x = 0.15$ mol% thus all of result is due to the conductivity of $x = 0.15$ mol% is maximum value as shown in Fig. 5.

3.2.5 Hopping carrier mobility and density

The hopping carrier mobility (μ) in the adiabatic and non-adiabatic hopping regions is described by the following equations [38]

$$\mu = \left(\frac{\upsilon_o e R^2}{kT} \right) exp(-W_H/kT) \qquad \text{(adiabatic)} \quad (24)$$

$$\mu = \left(\frac{eR^2}{kT} \right) \left(\frac{1}{\hbar} \right) \left(\frac{\pi}{4W_H kT} \right)^{1/2} J^2 exp(-E_a/kT) \quad (25)$$
(non-adiabatic)

In addition, the carrier density (N_c) values were calculated using the well-known relation [20]

$$\sigma = N_c e \mu \quad (26)$$

The values of μ and N_c (Eqs. 25 and 26, respectively) for various samples are presented in Table 4. The carrier mobility of the present system at 418 K is very small, suggesting that electrons are highly localized at the Fe^- ion sites, corresponding to the strong electron–phonon interacting the large γ_p [15]. Because the condition of the localized for the conductive electrons is generally for $\mu < 0.01$ $\mathrm{cm}^2\mathrm{V}^{-1}\mathrm{s}^{-1}$ [22], the formation of small polaron

Table 4 Hopping carrier mobility and density of $Bi_{1-x}Ba_xFeO_3$ multiferroic nanoparticles at fixed temperature (418 K)

x (mol%)	μ ($\mathrm{cm}^2\mathrm{V}^{-1}\mathrm{s}^{-1}$)	$N_c \times 10^{21}$ (cm^{-3})
0.10	2.39×10^{-7}	0.15
0.15	1.85×10^{-7}	1.11
0.20	1.32×10^{-11}	70.84
0.25	8.01×10^{-13}	34.03

in these samples was reconfirmed. In addition, the nearly constant of $N_c \sim 10^{21}$ cm^{-3} indicates that the conductivity of the samples is primarily determined by the hopping mobility [15].

4 Conclusion

A structural and transport properties of $BiBaFeO_3$ multiferroic nanoparticles samples have been reported systematically. We have succeeded in preparing $Bi_{1-x}Ba_xFeO_3$; ($x = 0.10$, 0.15, 0.20 and 0.25 mol%) multiferroic nanoparticles by solid-state reaction method. The lattice structure of the nanoparticles can be indexed to the hexagonal unit cell (with space group R3c). The density values of $BiBaFeO_3$ were found to be 7.76–8.17 g/cm^3 and the density decreased by increasing barium content. SEM micrograph appears an agglomeration process because of electrostatic potential and magnetic attraction. The activation energy of conduction for oxide semiconductors, which is the thermal energy required to hop the charges from one site to another. Thus, there is a strong correlation between the structural and electrical transport properties in this system. Dc conductivity shows that the maximum was found for $x = 0.15$ mol%. The values of electron–phonon interaction coefficient were large ($\gamma_p > 4$) usually indicate a strong electron–phonon interaction. The estimated hopping mobility was low 1.85×10^{-7} cm^{2}V^{-1}s^{-1} to 8.01×10^{-13} cm^{2}V^{-1}s^{-1} at fixed temperature (418 K) so the formation of small polaron in these samples was reconfirmed. The nearly constant of $N_c \sim 10^{21}$ cm^{-3} indicates that the conductivity is determined by the hopping mobility.

References

1. T. Kimura, S. Kawamoto, I. Yamada, M. Azuma, M. Takano, Y. Tokura, Phys. Rev. B **67**, 180401 (2003)
2. N. Hur, S. Park, P.A. Sharma, J.S. Ahn, S. Guha, S.W. Cheong, Nature **429**, 392–395 (2004)
3. M.A. Ahmed, E. Dhahri, S.I. El-Dek, M.S. Ayoub, Solid State Sci. **20**, 23–28 (2013)
4. G. Catalan, J.F. Scott, Adv. Mater. **21**, 2463–2485 (2009)
5. D. Varshney, A. Kumar, K. Verma, J. Alloys Compd. **509**, 8421 (2011)
6. D. Khomskii, Physics **2**, 20 (2009)
7. A.R. Makhdoom, M.J. Akhtar, M.A. Rafiq, M.M. Hassan, Ceram. Int. **38**, 3829–3834 (2012)
8. R. Das, K. Mandal, J. Magn. Magn. Mater. **324**, 1913–1918 (2012)
9. X.J. Xi, S.Y. Wang, W.F. Liu, H.J. Wang, F. Guo, X. Wang, J. Gao, D.J. Li, J. Magn. Magn. Mater. **355**, 259–264 (2014)
10. T. Holstein, Appl. Phys. (NY) **8**, 343 (1959)
11. S. Pal, A. Banerjee, E. Rozenberg, B.K. Chaudhuri, J. Appl. Phys. **89**, 4955 (2001)
12. M.M. El-Desoky, Phys. Status Solidi (a) **195**(2), 422 (2003)
13. M.M. El-Desoky, S.M. Abo-Naf, J. Mater. Sci. Mater. Electron. **15**, 425 (2004)
14. M.M. El-Desoky, I. Kashif, Phys. Status Solidi (a) **194**(1), 89 (2002)
15. M.M. El-Desoky, J. Mater. Sci. Mater. Electron. **14**, 215 (2003)
16. A. Al-Shahrani, A. Al-Hajry, M.M. El-Desoky, Phys. Status Solidi (a) **300**, 378 (2003)
17. M.S. Al-Assiri, S.A. Salem, M.M. El-Desoky, J. Phys. Chem. Solids **67**, 1873 (2006)
18. N.F. Mott, J. Non-Cryst. Solids **1**, 1 (1968)
19. M.M. El-Desoky, A. Al-Hajry, M. Tokunaga, T. Nishida, M.Y. Hassaan, Hyperfine Interact. **156/157**, 547 (2004)
20. I. Andelean, Solid State Commun. **27**, 697 (1978)
21. H.H. Qiu, H. Sakata, T. Hirayama, J. Chin. Ceram. Soc. **24**, 58 (1996)
22. N.F. Mott, E.A. Davis, *Electronic Processes in Non-Crystalline Materials* (Clarendon, Oxford, 1979)
23. Jaiparkash, R.S. Chauhan, Y. Kumar, N. Kumar, N. Vijayan, J. Alloys Compd. **598**, 248–252 (2014)
24. B. Yu, M. Li, J. Liu, D. Guo, L. Pei, X.Z. Zhao, J. Phys. D Appl. Phys. **41**, 065003 (2008)
25. B.D. Cullity, *Elements of X-ray Diffraction*, 2nd edn. (Addison-Wesley Publishing Company, Reading, MA, 1978)
26. S.J.L. Kang, *Sintering Densification, Grain Growth and Microstructure* (Elsevier, Oxford, 2005)
27. G. Biasotto, A.Z. Simões, C.R. Foschini, M.A. Zaghete, J.A. Varela, E. Longo, Mater. Res. Bull. **46**, 2543–2547 (2011)
28. A.Z. Simões, M.A. Ramírez, A.H.M. Gonzalez, C.S. Riccardi, A. Ries, E. Longo, J.A. Varela, J. Solid State Chem. **179**, 2206 (2006)
29. M.S. Al-Assiri, M.M. Mostafa, M.A. Ali, M.M. El-Desoky, Superlattices Microstruct. **75**, 127–135 (2014)
30. A. Al-Shahrani, M.M. El-Desoky, J. Mater. Sci. Mater. Electron. **17**, 43 (2006)
31. M.M. El-Desoky, A. Al-Shahrani, Phys. B **371**, 95 (2006)
32. N.F. Mott, Philos. Mag. **19**, 835 (1969)
33. A. Mukherjee, S. Basu, G. Chakraborty, M. Pal, J. Appl. Phys. **112**, 014321 (2012)
34. N.F. Mott, Adv. Phys. **16**, 49 (1967)
35. I.G. Austin, N.F. Mott, Adv. Phys. **18**, 41 (1969)
36. M.M. El-Desoky, M.S. Al-Assiri, A.A. Bahgat, A. Al-Hajry, J. Alloys Compd. **590**, 572 (2014)
37. H. Hirashima, D. Arai, T. Yoshida, J. Am. Ceram. Soc. **68**, 486 (1985)
38. A. Ghosh, J. Appl. Phys. **66**, 2425 (1989)